Constraining the Structure under Lunar Impact Basins with Gravity

David E Smith[1] , Sander Goossens[2] , Gregory A Neumann[2] , and Maria T Zuber[1]

[1] Department of Earth, Atmospheric and Planetary Sciences, Massachusetts Institute of Technology, Cambridge, MA 02139, USA; smithde@mit.edu
[2] NASA Goddard Space Flight Center, Solar System Exploration Division, Greenbelt, MD 20771, USA

Abstract

The lunar gravity field is used to estimate and constrain the depth of mass anomalies under 19 major lunar impact basins. We use radial gravitational spectra, consisting of accelerations computed either per spherical harmonic degree or cumulatively, at surface locations to obtain the distribution of the gravity signal with spherical harmonic degree and, by implication, to the likely depth below the surface. The results provide estimates for the maximum likely depths of the primary component to the mass anomalies under 19 basins. We find that the maximum depths of the primary source of mascon gravity on the lunar nearside are deeper than the depths for those on the farside when South Pole–Aitken (SPA) is excluded. All basin mass anomalies on the lunar nearside are in the mantle. The maximum depth of the primary source of the mass anomalies is <80 km, with the exception of SPA, whose dominant mass signature lies at a maximum depth of >200 km beneath the surface. The upper 20 km under all basins is largely devoid of anomalies, reflecting predominantly mixing and relaxation associated with impact melt combined with ejecta fallback, as well as homogenization associated with post-basin formation impact bombardment. Except for SPA, all basin anomalies merge with the deep interior at ~150 km or below, indicating the depth penetration of disruption of the density structure of the lunar interior associated with impact bombardment.

Unified Astronomy Thesaurus concepts: Lunar gravitational field (956)

1. Introduction

Knowledge of the interior structure of the Moon is of particular importance for understanding its formation and its consequent evolution, as well as that of the Earth–Moon system. Much of the understanding about Earth's and the Moon's interior comes from the interpretation of gravity, both surface measurements and those from spacecraft, often combined with topography. The combination of both provides strong constraints on its interior structure, especially that of the crust (Wieczorek 2015). For the Moon, recent measurements by lunar orbiting spacecraft, particularly the Gravity Recovery and Interior Laboratory (GRAIL) mission (Zuber et al. 2012), have provided high-resolution global gravity, and data from the Lunar Reconnaissance Orbiter Mission's Lunar Orbiter Laser Altimeter (Smith et al. 2016) have provided high accuracy and resolution topography. Their combination has been used to significantly improve our knowledge and understanding of the lunar crust, its density and porosity (Besserer et al. 2014; Milbury et al. 2015; Soderblom 2015), and its thickness (Wieczorek et al. 2013).

Our investigation uses Bouguer gravity, derived from free-air gravity and the topography, and in particular the distribution of Bouguer gravity with spherical harmonic degree under large impact basins with the goal to provide constraints on the depth of these anomalies. To relate spherical harmonic degree to depth, we use the relationship from Goossens & Smith (2023), which is derived by considering the gravity of a point mass and its spherical harmonic degree representation. The relationship

is expressed as

$$d = (1 - e^{\frac{-1}{L+1}})R, \tag{1}$$

where d is depth, R is the reference radius, and L is the spherical harmonic degree. For large degrees L this simplifies to

$$d = \frac{R}{L+1}. \tag{2}$$

As discussed in detail in Goossens & Smith (2023), the use of point-mass expressions poses limitations on its use when investigating complex realistic gravity signals. The inherent nonuniqueness of gravity means that such expressions can only be an approximation. In addition, any mass has power over the entire spherical harmonic spectrum (e.g., Pollack 1973; Sutton et al. 1991). The point-mass approximation then suggests a maximum depth of the anomaly of sorts (Dehlinger 1978; Goossens & Smith 2023). Thus, anomalies assigned to a depth based on degree can in principle also be caused by density anomalies that are shallower. In addition, it should be kept in mind that lower degrees can also, for a large part, be explained by relief along the crust–mantle boundary (e.g., Wieczorek & Philips 1998; Wieczorek et al. 2013). Nonetheless, expressions such as Equations (1) and (2) are useful to place (relative) bounds on masses, or to determine bounds for band-filtering gravity in order to probe a planet at different ranges of depths. Expressions such as Equation (1) and (2), and earlier ones such as that from Bowin (1983, 1986) (which resemble Equation (2); we refer to Goossens & Smith 2023 for details), have been used extensively in Earth and planetary sciences. These expressions can be especially useful to investigate well-defined anomalies, such as the mascons on the Moon, which show strong positive gravity anomalies. With these limitations in mind, we apply the point-mass relationship to well-defined anomalies and determine a maximum depth, resulting in relative depths for the
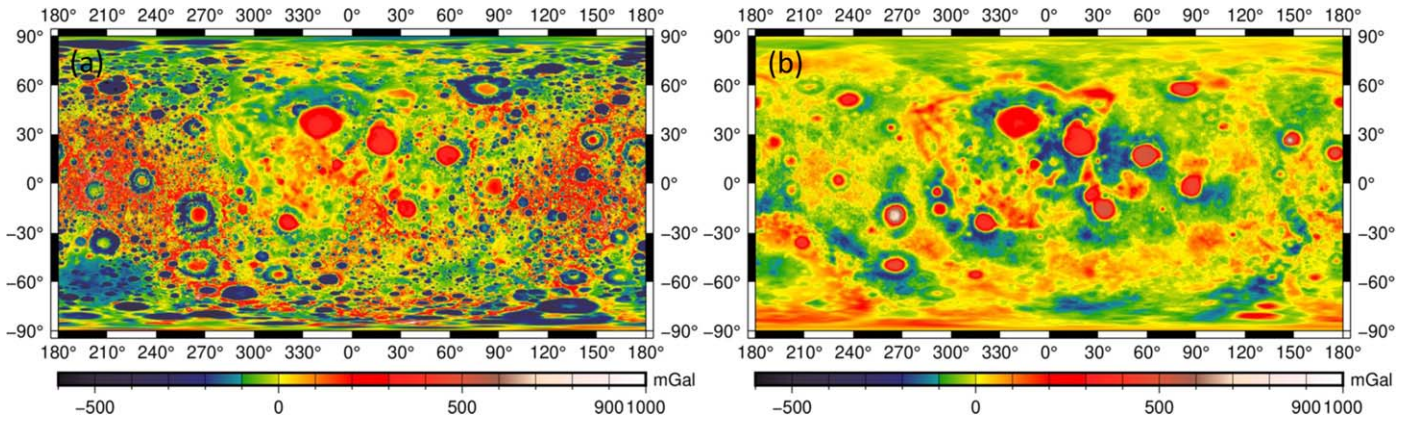
Figure 1. (a) Free-air gravity field (Equation (5)) of the Moon from GRAIL from the GRGM1200B model (Goossens et al. 2020) for degrees 2–600. (b) Bouguer gravity field based on GRAIL corrected for gravity from topography obtained by the laser altimeter (LOLA) instrument on the Lunar Reconnaissance Orbiter (LRO) spacecraft using a density of 2500 kg m^{-3} for the crust for degrees 6–600.

mass anomalies of these features. Finally, we note that when depth from a spherical harmonic degree L from Equation (1) is mentioned, we use "pm-km" in this paper, to underline that the depth has been derived from a point-mass relationship. Note that the surface resolution of anomalies, as opposed to depth, is derived from half-wavelength resolution of spherical harmonics. The latter is derived from the half-wavelength resolution of spherical harmonics λ_{half}, which is (approximately) related to degree following

$$\lambda_{half} = \frac{\pi R}{L}. \tag{3}$$

This describes the resolution at the surface in km at the equator and results in different values from the depth derived from Equation (1). For example, at $L = 180$ the surface resolution is ∼30 km, but the depth from Equation (1) would be ∼10 km.

The interior structure of the Moon has long been a subject of study, especially with the high-resolution gravity and topography data from GRAIL and LOLA (Andrews-Hanna et al. 2013; Wieczorek et al. 2013; Zuber et al. 2013). Studies have focused on global density variations both laterally and vertically (Besserer et al. 2014; Han et al. 2014) and the thickness of the crust (Wieczorek et al. 2013). Smaller-scale density variations have also been studied (Andrews-Hanna et al. 2013; Jansen et al. 2017), as well as the larger Procellarum area (Andrews-Hanna et al. 2014) and South Pole–Aitken (SPA; James et al. 2019). The Orientale basin, the youngest large impact basin on the Moon, was of special interest, as GRAIL collected data over the basin at 5 km over the rim and ∼12 km over the basin floor (Zuber et al. 2016; Andrews-Hanna et al. 2018).

Of particular interest for this work are several studies of the density structure of the Moon using inversions of gravity, with a special focus on the mascons. Short for mass concentration, these are features of topographic lows but with gravitational highs, first discovered in the pre-Apollo lunar exploration era (Muller & Sjogren 1968). Data from GRAIL finally revealed their origin as resulting from isostatic adjustment, cooling, and contraction of melt after impact (Melosh et al. 2013). GRAIL gravity data were used to constrain their structure expressed in terms of density contrasts at depth (Liang et al. 2014; Zhao et al. 2019, 2021). These studies invert gravity for density contrasts, which is well known to be an ill-posed problem suffering from nonuniqueness. Several constraints were thus

applied, based, for example, on the method of Li and Oldenburg (1998), where depth-weighting is used to avoid placing all density contrasts close to the surface (which is a natural result in unconstrained inversions owing to the attenuation of gravity with increasing distance). These studies place most density contrasts at the base of the crust, using different ranges of band-filtered Bouguer gravity for the inversion. For example, Liang et al. (2014) limited their input signal to degree 60, whereas Zhao et al. (2019) used up to degree 720 at 1748 km, and Zhao et al. (2021) inverted gravity between degrees 6 and 450.

Our approach here is different from these inversions. We aim to constrain depth, not the density contrast itself, from gravity without depth constraints, by focusing on the variations of Bouguer gravity per spherical harmonic degree. Since a spherical harmonic can be related approximately to depth (Bowin 1983, 1986; Goossens & Smith 2023), the gravity field can provide data on how mass might be distributed in the planet's interior. This information can be particularly interesting for large impact basins, which generally exhibit large gravity anomalies (Figure 1(a)). As noted before, the lower degrees of the gravity field also play a large part in determining the global relief along the crust–mantle interface, and this should be kept in mind when interpreting these degrees. Our focus, however, is to investigate the Bouguer gravity signal at particular locations. This is different from the determination of crustal thickness where the Bouguer anomaly is downward continued and minimized (e.g., Wieczorek & Philips 1998). The fact that the crust–mantle relief explains a large part of the lower degrees may contribute to uncertainty about the absolute depth of anomalies (in addition to the approximations using point masses). As we will show, however, our results match well with those from other inversion techniques.

In this paper we investigate the gravity fields of 19 impact basins at points within and around them, and in Section 3.1 we compare the results with the locations of density anomalies beneath major basins by Liang et al. (2014) and Zhao et al. (2021).

This paper is organized as follows: Section 2 provides our approach; Section 3 provides an interpretation of gravity spectra, including depth constraints (Section 3.1), horizontal constraints (Section 3.2), SPA (Section 3.3), and hemispheric comparisons (Section 3.4); Section 4 provides a summary of the spectral method and assumptions; and Section 5 provides a summary of observations and conclusions.

2. Approach

2.1. Gravitational Spectrum at a Point Location in SPH

The gravity field at a point on the surface of a planetary body can be expressed as a series of spherical harmonics. In geodesy it is common to work with a disturbing potential T, which is the difference between the full gravitational potential and a normal potential of a reference ellipsoid. The disturbing potential does not include the potential induced by the rotation of the body. It can be expressed in spherical harmonics of degree l and order m following (e.g., Heiskanen & Moritz 1967)

$$T(r, \lambda, \varphi) = \frac{GM}{R} \sum_{l=2}^{\infty} \left(\frac{R}{r}\right)^{l+1}$$
$$\times \sum_{m=0}^{l} (\bar{C}_{lm} \cos m\lambda + \bar{S}_{lm} \sin m\lambda) \bar{P}_{lm}(\sin \varphi), \qquad (4)$$

where (r, λ, φ) are the spherical coordinates radius, longitude, and latitude, respectively, of the point where the potential is to be computed; R is the reference radius of the body; $\bar{C}_{lm}$ and $\bar{S}_{lm}$ are the coefficients of the gravity field model; and $\bar{P}_{lm}$ are the associated Legendre functions. The bar indicates normalized coefficients, and we use the standard 4π normalization (e.g., Kaula 1966). In this work, we mostly focus on the radial acceleration δg, which is defined as

$$\delta g = -\frac{\partial T}{\partial r}, \qquad (5)$$

which can be expressed in spherical harmonics as

$$\delta g(r, \lambda, \varphi) = \frac{GM}{R^2} \sum_{l=2}^{\infty} \left(\frac{R}{r}\right)^{l+2} (l+1)$$
$$\times \sum_{m=0}^{l} (\bar{C}_{lm} \cos m\lambda + \bar{S}_{lm} \sin m\lambda) \bar{P}_{lm}(\sin \varphi). \qquad (6)$$

In this work, we use variations of Equation (6). Obviously, there is a maximum degree instead of infinity for the summation. We call Equation (6) expressed up to a fixed degree L cumulative gravity, $\delta g_c(L)$. If we define a maximum degree L_{marex} that we use in our expansions, then we can also use Equation (6) to compute gravity from a starting degree L up to L_{max}. We call this cumulative-reverse gravity $\delta g_r(L)$, because in keeping the maximum degree fixed, we count down over degree values L. Finally, we can compute Equation (6) for one degree value L only. We call this individual (degree) gravity $\delta g_i(L)$, and we include the equation here,

$$\delta g_i(r, \lambda, \varphi)(L) = \frac{GM}{R^2} \left(\frac{R}{r}\right)^{L+2} (L+1)$$
$$\times \sum_{m=0}^{L} (\bar{C}_{lm} \cos m\lambda + \bar{S}_{lm} \sin m\lambda) \bar{P}_{lm}(\sin \varphi). \qquad (7)$$

For our applications, we compute gravity accelerations at the reference surface, which implies that R equals r, unless stated otherwise.

We make the distinction between cumulative and cumulative-reverse in light of the degree–depth relationship of Equation (1). If we relate L to depth in this way, one can view cumulative gravity as being built up from the deep interior (starting at degree $l = 2$, which is at depth), whereas

cumulative-reverse gravity can be viewed as starting closer to the surface (depending on the value of L_{max}, which we choose to be as large as the global models allow). Individual gravity spectra may be more difficult to interpret, but they are essentially the raw data for this study and contain information intrinsic to the gravity of the Moon. We view it as providing information at a certain depth, keeping in mind of course that the degree–depth relationship is an approximation. We also note that cumulative gravity and individual gravity are related, where individual gravity can be seen as a (scaled) derivative of cumulative gravity, because $\delta g_i(L) = \delta g_c(L) - \delta g_c(L - 1)$.

We use the GRGM1200B gravity model (Goossens et al. 2020; Figure 1(a)) and focus on Bouguer gravity computed from this model using LOLA topography following Wieczorek & Philips (1998), assuming a density of 2500 kg m^{-3} for the crust (Figure 1(b)). The spectrum of each profile is derived for all degrees from 2 to 1200.

In Figure 2 we show the full individual Bouguer spectra for 19 impact basins: Apollo, Crisium, Dirichlet–Jackson, Grimaldi, Hertzsprung, Humorum, Imbrium, Korolev, Mendel–Rydberg, Moscoviense, Nectaris, Nubium, Orientale, Planck, Poincare, Schrodinger, Serenitatis, Smythii, and SPA. In addition, Figure 2 shows the average spectrum for approximately 15,000 locations on the Moon where the Bouguer anomaly is zero ± 1 mGal (for the degree range 6–600). The locations are along the yellow-green intersection on Figure 1(b) and include the transitions between high and low regions on basins, as well as "smooth" areas. We also developed the average for the area without mascons by excluding locations that are within 1.5 times the radius of the largest mascons on the Moon and found the largest magnitude difference to be approximately 50% smaller at $L = 20$; otherwise, the difference was negligible at both higher and lower degrees. We refer to this spectrum as "Zero" and describe it as the "normal" Moon in the absence of impacts and other gravity disturbances that produce heterogeneities in internal structure. Our spectra are hence an indication of the degree to which disturbances in the Moon's mass are frozen into the lithosphere.

Features that are seen in the individual spectra (Figure 2) include quasi-oscillations, a near-permanent departure from zero at lower degree $L \sim 50$ before returning to near zero around $L = 5$–10, and an increase in scatter at about $L = 800$, all of which are discussed in detail later.

For many of the basins in Figure 2 in the degree range $L > 30$ there are small oscillations about zero. Good examples are Crisium, Nectaris, Serenitatis, and Smythii, all on the nearside, but other basins suggest that they might also exhibit similar oscillations. An additional feature is the departure from zero mGal seen in some basins, such as Imbrium, Mendel–Rydberg, and Orientale. This feature also is seen, and much more clearly, in Figure 4 (showing the cumulative spectra), where we identify it as the transition level. We discuss the possible causes for the oscillations and the transition level later in Section 2.2.

At $L = \sim 800$ in Figure 2 the signal increases and data noise from the gravity field model is expected to be a major contributor. Figure 3 (left) shows the geographical distribution of the Bouguer gravity signal for $L = 700$–1200 and $L = 1000$–1200, indicating that most of the signal above $L = 700$ originates in the lunar highlands from degrees 1000 to 1200, but also showing Dirichlet–Jackson, Hertzsprung, and
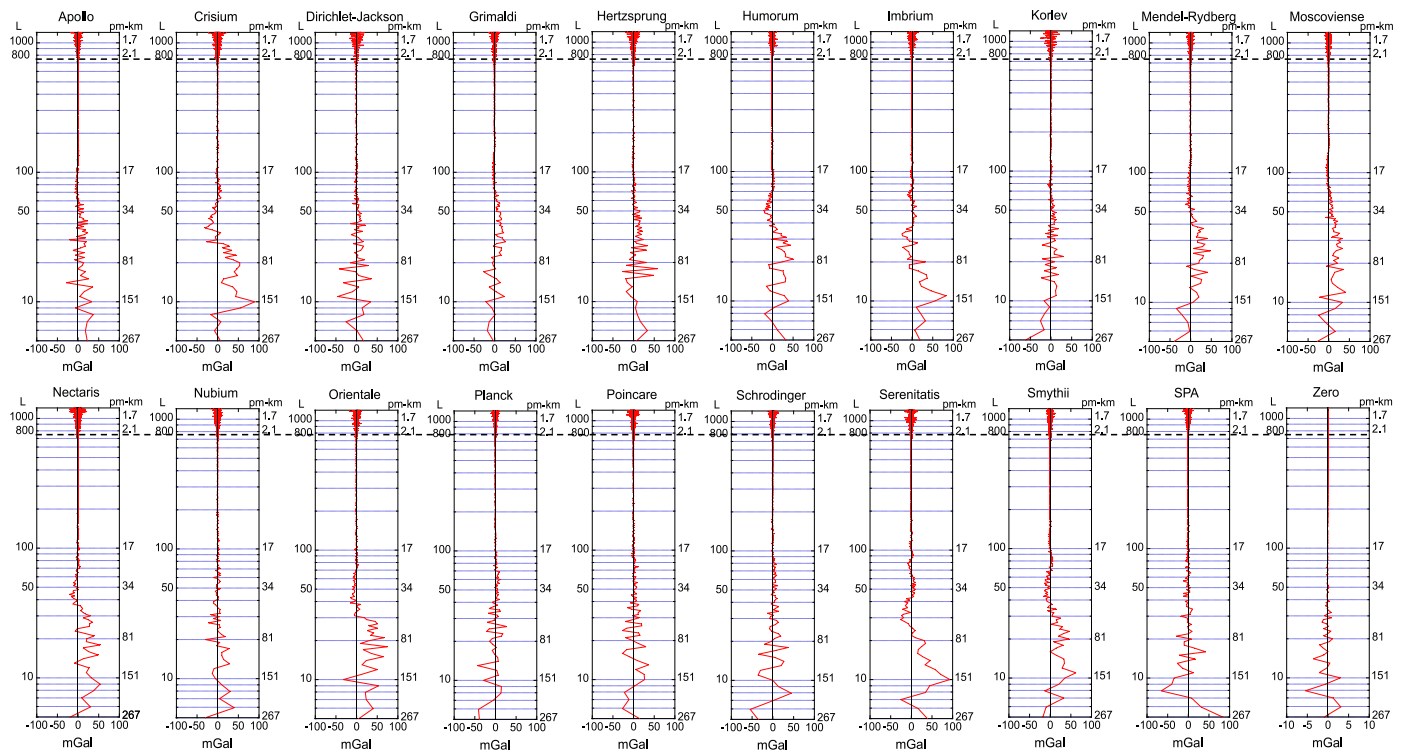
Figure 2. Bouguer gravity individual spectra of 19 basins and the average spectrum ("Zero") of over 15,000 locations where the Bouguer gravity was between ±1 mGal. All individual figures are on the same horizontal scale ±100 mGal except Zero, which is ± 10 mGal. The left axis of the spectra is spherical harmonic degree L, right axis pm-km. The spectra show limited anomalous signal between spherical harmonic degree $L \sim 100$ and ~ 700, representing a depth of 2.5–17 pm-km, the upper crust. The region $L > 800$ is a combination of data noise and possibly gravity signal from the top 2–3 km of the crust. All spectra are evaluated at the central location of the feature, at the reference radius of 1738 km. Note that the vertical axis (degree, L) is logarithmic.
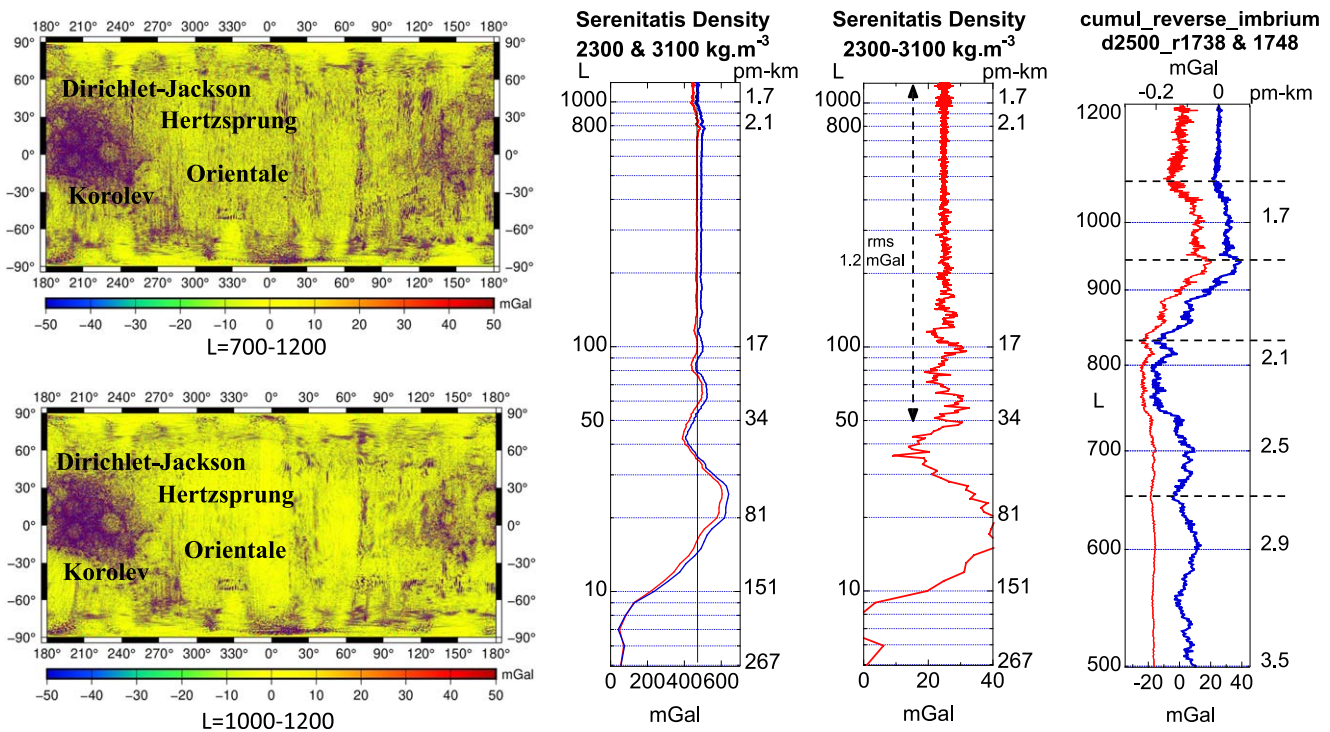

Figure 3. Left: the geographical distribution of Bouguer gravity signal for $L = 700$–1200 and 1000–1200 degrees for crustal densities of 2500 kg m^{-3}. Right: two cumulative spectra of Serenitatis for different densities, and two cumulative-reverse spectra for Imbrium at different radii. The two cumulative profiles on the left compare densities of 2300 and 3100 kg m^{-3}; the third cumulative-reverse profile compares the effect of evaluating the Bouguer field at 1738 and 1748 km approximately equivalent to the elevation on the lunar nearside and farside. The third profile has a double X-axis where the lower X-axis is 1738 km (red data) and the upper X-axis is 1748 km (blue data).

Korolev visible in both degree ranges. No coherent signal is identifiable on the lunar nearside, probably due to the lack of significant topography over large areas and the greater distance to the reference surface than on the farside.

The right column of Figure 3 shows two cumulative spectra for Serenitatis for two different crustal densities and their difference, indicating the almost identical nature at both densities (thus establishing that a different local density does not alter the shape of the curves), and two spectra of Imbrium for $L = 500–1200$ showing the small, near-constant magnitude over all degrees, particularly for $L > 50$. Imbrium spectra are cumulative-reverse ones for two reference radii, 1738 and 1748 km, for a density of 2500 km.m^{-3}, showing that the inflection points of the two spectra occur at the same degree L and pm-km, irrespective of the reference radius.

It is known that referring to a sphere that does not encompass the entire mass of the Moon has an effect on the high-degree coefficients (Šprlák & Han 2021), but our results using the different reference radii suggest that the effect is largely in the magnitude of the signal, not its character.

The farside signal seen in the left column of Figure 3, coupled with the indication from the Imbrium spectra suggesting that the reference radius largely only affects the magnitude of the anomaly, suggests that we may tentatively conclude that there could be some evidence of genuine gravity signal in addition to data noise present in the degree range $L = 700–1200$, particularly for the farside highlands.

Most of the signal in the global maps for $L > 700$ is largely restricted to the lunar highlands with several basins evident; the small difference in the chart suggests that data noise is a significant contributor in the 1000–1200 degree range. The left profile comparing two densities indicates a very similar variation for all L and depths. The middle profile shows the difference between the two densities, and the rms difference for $L = 50–1200$ is only 1.2 mGal on a signal of approximately 500 mGal. The right (cumulative-reverse) profile indicates that the peaks and troughs in the profiles are occurring at the same degree and depth, shown by the black dashed lines, and independent of the reference radius.

Although buried mass anomalies (Evans et al. 2016) were found to be as thick as 7 km and thus possibly within our range of depths that we analyze, we do not include them in our study, as they relate to nearside maria. Here we focus on the structure of large basins and on the degree range where correlations with topography are uniformly high. We leave in-depth discussion of the higher degrees, which relate to, for example, mare deposits and cryptomare (Gong et al. 2016; Sori et al. 2016), for future research.

2.2. Accumulation of Gravity

The cumulative gravity signal from $L = 5$ to $L = 1200$ is shown in Figure 4 for the same basin anomalies as in Figure 2. Each spectral value is evaluated at the reference radius of 1738 km. For many accumulated spectra there is a sinusoidal pattern that starts at degree $L \sim 10$, continuing to higher degrees and eventually increasing almost monotonically to degree ~ 100, where the anomaly signal stabilizes to the surface. This is the same oscillation seen in Figure 2 manifest in the cumulative spectra shown here. In Figure 4 the oscillation is seen more clearly. There is a possibility that this oscillation is the result of ringing (such as truncation effects of spherical harmonics) and thus not physical. Additional tests with a synthetically created

buried mass, however, show ringing effects in images of band-filtered gravity signal (see also Section 3.2 for a discussion of such images for some of the basins under consideration). However, those are not correlated with the size of the synthetic anomaly at the surface, but more indicative of the possible depth, which is how we interpret the cumulative spectra.

Figure 4 shows constant values from $L \sim 100$ to ~ 800 (2.2–17.1 pm-km) for all basins. Basins that exhibit no significant increase or decrease in this range include Crisium, Grimaldi, Moscoviense, and Smythii, all of which are distributed in longitude. This possibly indicates mixing and relaxation of the near surface (e.g., Zuber et al. 2013) with post-basin formation. The dashed black line in Figure 4 is the depth location where the main contribution to the value at the surface originates; we call this the transition depth and discuss the definition and interpretation in more detail in Section 3. This level is also seen in Figure 2, where the individual spectra cross zero before rising and subsequently descending in the 10–20 degree band.

The sinusoidal oscillation in Figure 4, mentioned above, is not consistent across all basins. It could be the result of truncation of the spherical series in forming the cumulative spectra, but all cumulative spectra are derived in the same manner, and not all spectra show the oscillation. In addition, the oscillation is also seen in some of the individual spectra. In order to better understand how truncation would affect the spectra, we investigated the spectra of free-air gravity and gravity from topography.

Figure 5 shows this comparison for eight anomalies, four on the lunar nearside and four on the lunar farside. The figure shows how the free-air spectra are highly variable, as is the topographic correction, but the resulting Bouguer is usually smooth and removes nearly all the shorter-wavelength features, as is to be expected because gravity and topography are highly correlated. The effect of the topography is seen to propagate through the complete spectrum, and both the free-air and the gravity from topography show near-identical oscillations that cancel in the Bouguer. The remaining oscillations in the Bouguer spectra could be because the feature is starting to be resolved as the degrees increase from $L = 2$, and this should also be seen in the gravity from topography spectra. However, at low degrees both gravity and topography are well determined, and Figure 5 shows their strong correlation (or anticorrelation in the case of mascons), with indeed oscillations in both gravity and gravity from topography leaving only smaller oscillations in the Bouguer, which we consider as indicative of density variations at depth.

Figure 6 presents examples of four anomalies for degree ranges 900–1200, each with different characteristics. Each of the examples appear to be composed of at least two distinct frequencies, a low frequency and at least one high frequency. Since Figure 6 corresponds to depths of 1–2 pm-km, we consider it likely that the patterns seen are a manifestation of data noise and leave further analysis of the high-degree data for future work.

The previous spectra, individual and cumulative, correspond to the central point of the anomaly. We have also developed meridional profiles of spectra for six basins that show how the spectra vary with location within and across the basin. Figure 7 shows the integrated spectrum spaced every 1° of latitude through four anomalies from degrees 5 to 1200 for Imbrium, Crisium, Smythii, and Moscoviense. Figure 8 shows spectra of
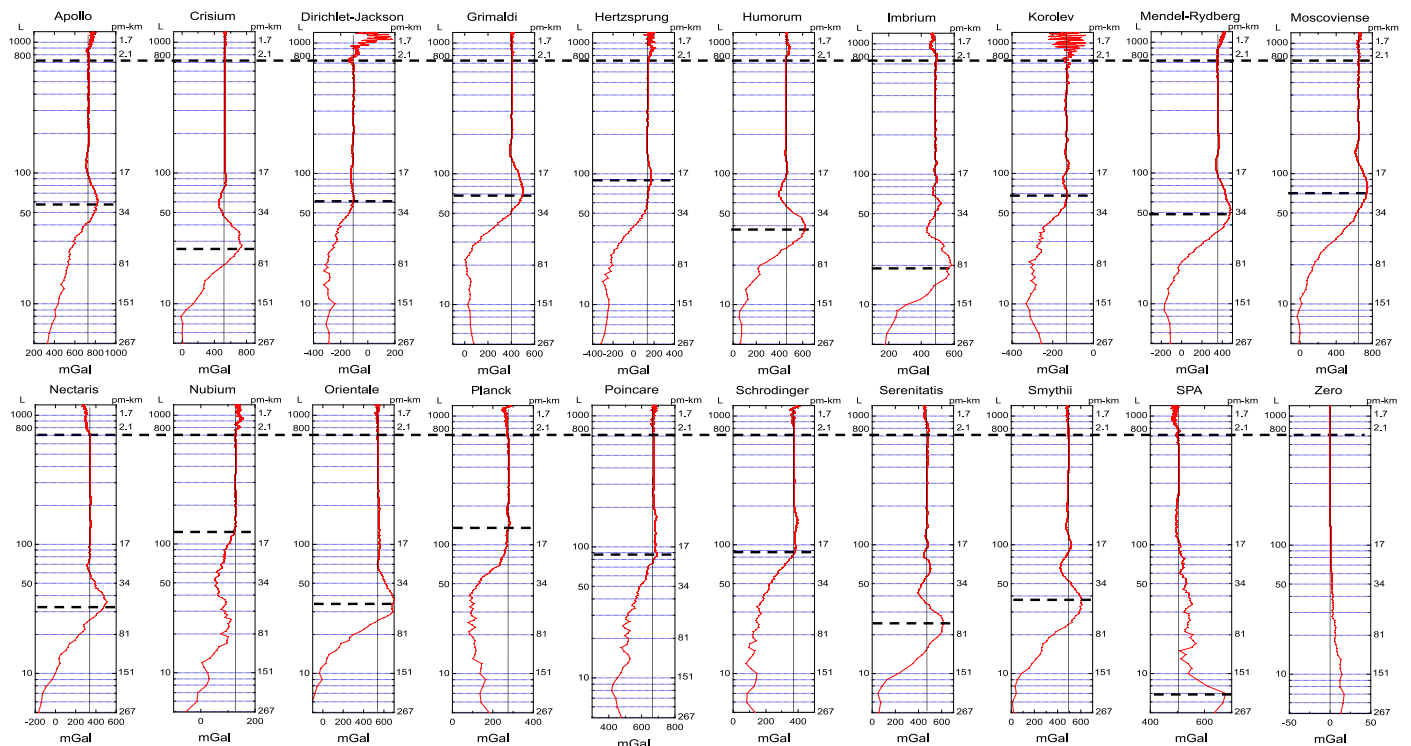
Figure 4. The cumulative Bouguer gravity from $L = 5$ to 1200 shows how gravity changes with depth below the surface, highlighting the increase in signal variation approaching the surface for all basins. The Zero profile also decreases, but the magnitude is minimal compared to the basins. The dashed lines indicate what we call the "transition depth" (see also Section 3), where the maximum is followed by a decrease as the depth increases. The transition depth is the depth at which most of the observed cumulative Bouguer gravity signal at the surface originates. The accumulated spectral values are computed at the reference radius of 1738 km.
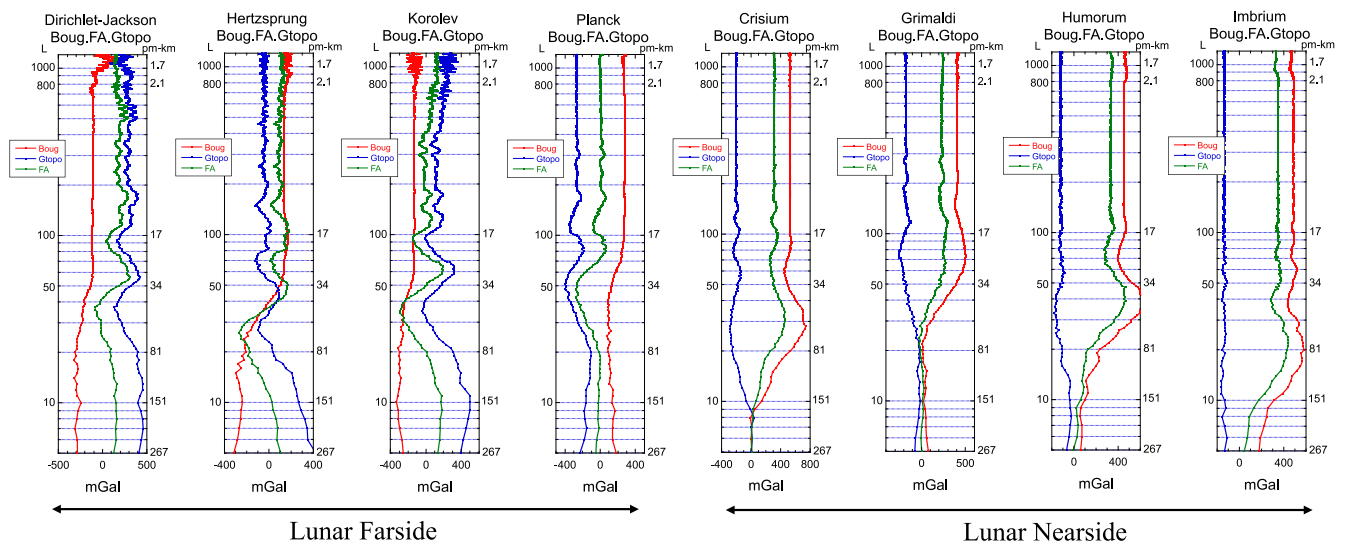

Figure 5. Comparison of eight profiles of Bouguer (red), gravity from topography (blue), and free-air gravity (green). The Bouguer profiles and the free-air gravity profile corrected for topography are invariably smoother than the free-air and show how significant the topography can be on the free-air gravity field at most wavelengths. We note the smooth nature of all spectra of the four nearside basins compared to the variations seen in the farside basins, most likely due to the large topographic variations in the highlands. Nevertheless, the resulting Bouguer is smooth for $L < 800$ (~3 pm-km).

profiles through Orientale and Mendel–Rydberg from the equator to 80°S along 266°E longitude.

The cumulative spectra in Figures 7 and 8 all exhibit the same pattern: starting at $L = 500$ (~3 pm-km), the spectra are near constant and then decrease slightly before rising to a maximum value at the transition level and rapidly decreasing to converge at around $L = 10$, ~150 pm-km, or at slightly greater depth. At these lower degrees we suggest that the anomaly no longer has any signal that contributes to the anomaly value at

the surface and that at the lower degrees the spectra are merging with the long-wavelength gravity of the deep interior that contributes to the gravity of the region. We corroborate this finding in Section 3.2, where we discuss horizontal maps of accelerations, band-filtered for a range of degrees, which we refer to later as "slices."

Figure 8 shows the meridional profile 266°E from the equator to latitude 70°S, passing though both the Orientale and Mendel–Rydberg basins. The figure shows the almost
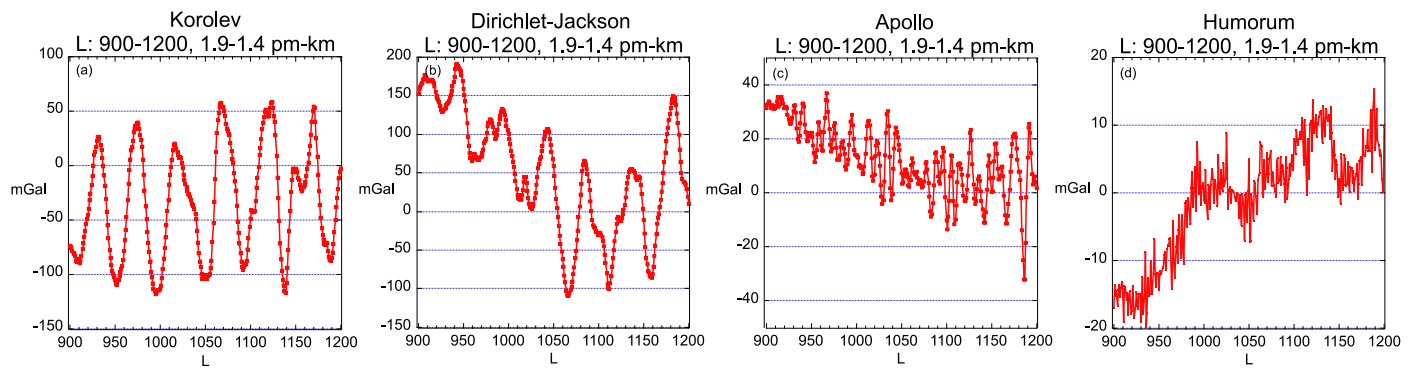
Figure 6. Four examples of gravity signal spectra for $L = 900$–1200, a region that we expect to contain significant data noise that manifests itself in different forms. The charts for (a) Korolev and (b) Dirichlet–Jackson suggest possible short-wavelength variations, while the charts for (c) Apollo and (d) Humorum show long-wavelength trends.
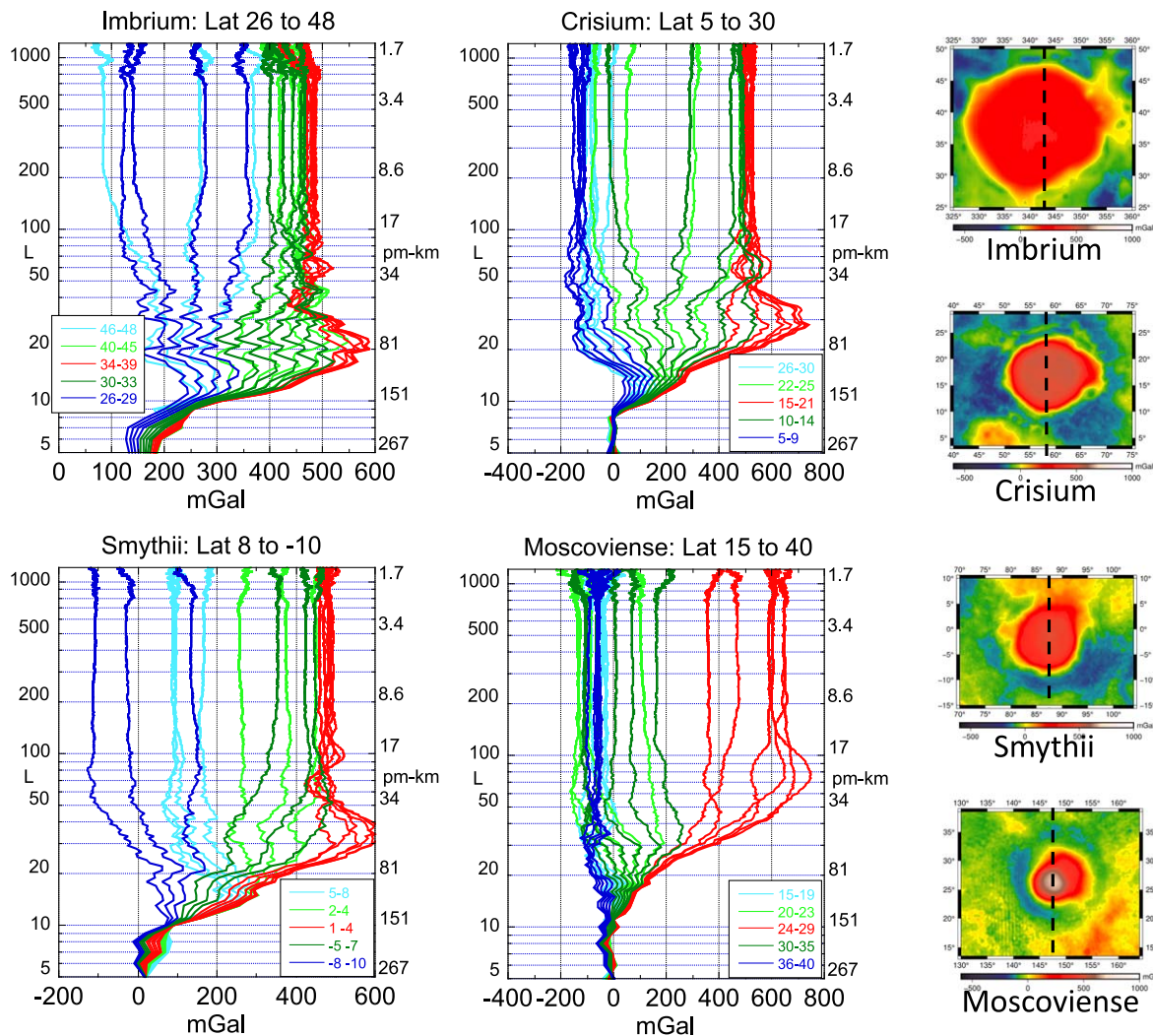

Figure 7. Profiles in latitude across four basins, Imbrium, Crisium, Smythii, and Moscoviense, showing the variation of spectra with degree L and depth (pm-km), and latitude. Each profile set crosses the northern moat, the central high, and the southern moat. The light-blue region is the northern region that includes the moat, the light-green region covers the region prior to the central core, the red region indicates the central core, the dark-green region is the edge of the core prior to the moat, and the dark-blue region includes the southern moat. Each basin shows a maximum in the $L = 20$–60 degree range, $\sim$30–80 pm-km depth. Note: all spectra begin to diverge at $L \sim 10$, $\sim$150 pm-km, and reach an almost constant value at $L \sim 100$, 17 pm-km. Thumbnail images of the gravity disturbance of each basin are shown on the right for degree ranges 6–600.

undisturbed "normal" spectra before, between, and beyond the basins. The four panels are on the same longitude scale, emphasizing the differences along the meridian. The spectra between the basins are almost constant for 6° of latitude,

suggesting that although both basins are geographically close, they are for the most part gravitationally distinct. However, we note that the signal value is –200 mGal in the –35° to –40° latitude band between Orientale and Mendel–Rydberg and is
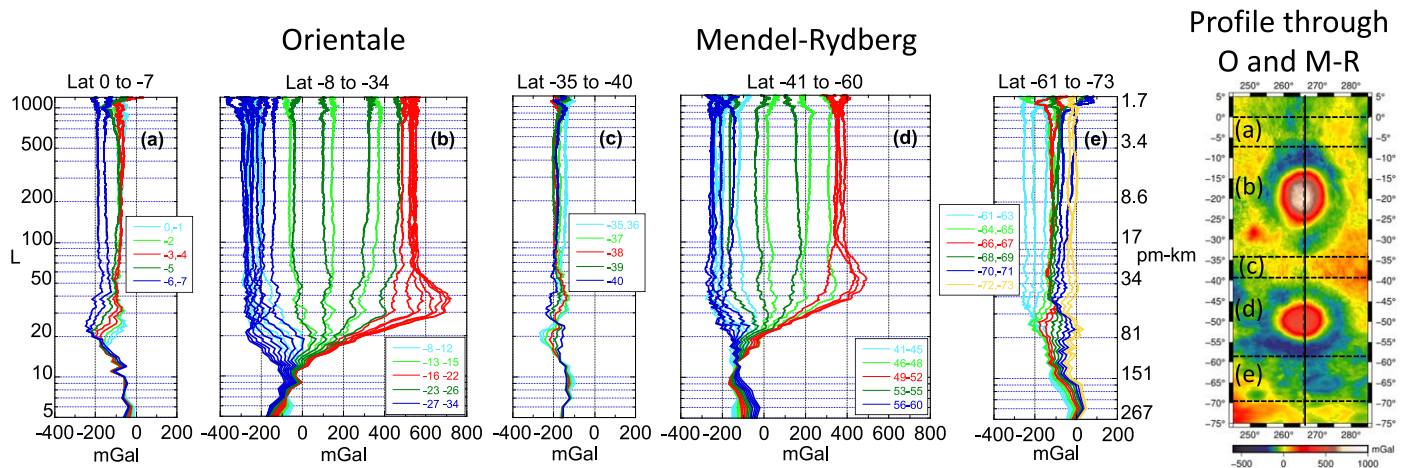
Figure 8. Profile of cumulative spectra from equator to 70°S along 266°E longitude. The profile crosses through Orientale and Mendel–Rydberg basins. The profile colors indicate the latitude range of each section: light blue is the northern end of the profile, red the central core, and dark blue the southern end of the profile. Light green and dark green show the intermediate regions between the northern and southern moats and the central core, where appropriate. Spectra show that the region north of Orientale (panel (a)) is near constant from $L = 20$–800 and decreases as it enters in the northern moat (panel (b)) and crosses onto the central high, increasing to a maximum and then decreasing into the southern moat and into the region between the basins (panel (c)), where the signal is again near constant. The profile crosses into the northern moat of Mendel–Rydberg (panel (d)), increases onto the basin high and through the southern moat where the spectra are largely constant, and into the region (panel (e)) to the south. Similar to the basins in Figure 6, the gravity maxima are in the $L \sim 40$–50 degree range.

offset from the Zero spectra in Figure 7. This could indicate some overlap of the Orientale and Mendel–Rydberg fields.

3. Interpretation of Gravity Spectra

3.1. Depth Constraints on the Lunar Interior Structure

The correlations of free-air gravity and Bouguer gravity with gravity from topography provide an indication of the range of degrees (L) over which gravity can be reliably interpreted. Figure 9 shows this correlation for $L = 10$–1200 for both free-air and Bouguer, indicating that at degree 900 the correlation is >0.5 for free-air and $\sim$–0.2 for Bouguer, suggesting that at this degree and resolution the Bouguer gravity is probably reliable and independent of topography despite the possible increase in data noise at $L = 800$ seen in Figure 3, corresponding to a depth of $\sim$2.2 pm-km. The trend in Bouguer correlations is due to assuming a constant density in the crust; this trend disappears when we account for vertical density variations (Han et al. 2014). However, we find that our profiles are not affected by using this different way of computing the Bouguer correction.

At the lowest degrees the correlation between free-air and topography is very low, but at these degrees the gravity coefficients are the most accurate and the lack of correlation with topography, largely due to the presence of the large basins on the lunar nearside, does not affect the interpretation of the Bouguer gravity at these lower degrees.

A common characteristic in all individual spectra (Figure 2) is an effectively zero anomalous signal in the degree range $L = 700$–100 with a few exceptions, a depth range of 2.5–17 pm-km that suggests a $\sim$15 pm-km homogeneous region under most major basins. The average spectrum of all 15,000 zero value surface anomalies indicates that this feature extends to $L \sim 50$, $\sim$34 pm-km, probably related to the average thickness of the lunar crust homogenized by impacts, and in agreement with the results from GRAIL analyses (Wieczorek et al. 2013; Zuber et al. 2013).

Another feature that appears in many but not all basin spectra is the oscillation that begins beneath the upper crustal layer ($L \sim 100$, $\sim$17 pm-km) increasing in amplitude with decreasing
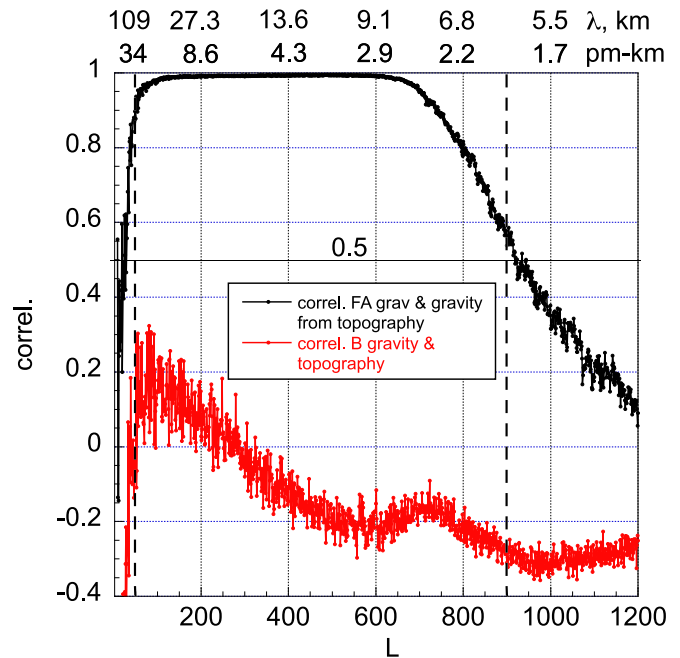

Figure 9. Correlation of free-air gravity (FA) with topography (black) and Bouguer (B) gravity with topography (red). Vertical dashed lines delimit the range of degrees over which gravity is highly correlated with topography. The plot indicates that at degree 900 (<2 pm-km) the FA gravity and Bouguer gravity are both uncorrelated with topography. The upper axis shows the pm-km, and λ, km, the surface resolution.

degree and greater depth. This oscillation is clearly seen in the Imbrium and Smythii spectra.

Another feature appearing in many of the individual spectra (Figure 2) is a large increase in magnitude beginning at $L = \sim 60$ (28 pm-km). This feature is more evident in Figure 4, where the maximum signal for the majority of the integrated spectra is followed by a decrease to about $L = 10$ (151 pm-km). Because of the difficulty of deriving this location (in L or km) for Planck and Korolev, and possibly Schrodinger, we selected the largest mGal value in all the cumulative spectra in the range

Table 1
Parameters of the Basins Used in This Study and Location of the Transition in Spherical Harmonic Degree *L*, and pm-km, Along with Estimates of Their Uncertainties

#	Basin	lon	lat	diam	cr.thick	age	trans.L	trans.pm-km	trans.mGal	Liang.km	Zhao.km
1	Apollo	208.28	−36.07	264.0	3.91	1	61 ± 2	27.8 ± 1	822 ± 2		
2	Crisium	58.40	16.80	498.0	3.60	2	28 ± 1	58.9 ± 2	741 ± 4	20–50	20–60
3	Dirichlet–Jackson	201.84	13.45	220.0	39.19	1	66 ± 2	25.8 ± 1	−104 ± 2		
4	Grimaldi	291.31	−5.01	220.0	8.49	1	73 ± 2	23.3 ± 1	503 ± 1		
5	Hertzsprung	230.84	2.02	254.0	19.46	2	95 ± 4	18.0 ± 1	175 ± 2		
6	Humorum	320.80	−23.80	360.0	9.04	2	37 ± 3	45.1 ± 4	622 ± 4	…	18–50
7	Imbrium	341.50	37.00	684.0	10.09	3	20 ± 2	80.8 ± 8	587 ± 9	20–50	20–50
8	Korolev	202.20	−4.44	202.0	38.04	2	73 ± 2	23.3 ± 1	−127 ± 2		
9	Mendel–Rydberg	265.40	−49.80	328.0	13.65	2	53 ± 2	31.9 ± 2	484 ± 3	20–40	18–50
10	Moscoviense*	147.00	26.10	300.0	1.46	2	78 ± 2	21.9 ± 1	750 ± 2	…	18–80
11	Nectaris	35.10	−15.60	440.0	8.65	2	36 ± 2	46.3 ± 3	507 ± 4	…	20–60
12	Nubium	343.40	−21.30	416.0	24.97	1	136 ± 4	12.6 ± 1	129 ± 1		
13	Orientale	265.20	−20.10	436.0	7.96	3	38 ± 5	44.0 ± 8	707 ± 10	20–40	18–70
14	Planck	135.09	−57.39	128.0	16.65	1	148 ± 2	11.6 ± 1	284 ± 1		
15	Poincare	163.15	−57.32	188.0	4.03	1	87 ± 2	19.6 ± 1	693 ± 2		
16	Schrodinger	133.53	−74.86	154.0	7.46	3	90 ± 4	19.0 ± 1	385 ± 2		
17	Serenitatis	18.80	25.40	556.0	6.85	2	25 ± 2	65.6 ± 5	615 ± 7	20–50	20–50
18	Smythii	86.90	−2.50	438.0	6.13	1	34 ± 3	49.0 ± 4	608 ± 5	20–50	25-60
19	South_Pole_Aitken**	191.00	−53.00	2050.0	15.16	1	7 ± 1	204.2 ± 25	678 ± 8		

Notes. The depths in red indicate when the transition depth is outside the range from Liang et al. (2014) and Zhao et al. (2021). Reference position of basins is from Neumann et al. (2015) (except SPA), crustal thickness from Wieczorek et al. (2013), and the age from Losiak et al. (2009).
[a] Diameter estimated from Bouguer plot of Neumann et al. (2015).
[b] Diameter from topography.

$L = 5$–500 and assigned this the "transition depth." We hypothesize that the transition depth represents the location where primary gravity signal observed at the surface originates, and subsequently begins to merge with the deeper structure of the mantle. In addition, as we will show below, there is also a clear relationship between the transition degree and surface resolution, as both depth and surface resolution are roughly proportional to $1/L$ (see Equations ((2) and (3)). This means that the transition degree can also be viewed as the degree at which the feature is starting to be resolved at the surface. Our interpretation is that it can also be related to depth and that the transition degree thus provides information about the maximum depth of the mass anomaly. Because we use our point-mass relationship to relate the spherical harmonics degrees to depth, the transition depth may only be an approximation of the true depth. But because we determine the transition depth for each profile in the same way, at the least they provide relative depths among the basins.

The locations of the changes with depth are shown in Figure 4 by dashed lines for 19 basins; the "Zero" spectrum does not show a transition depth. On the depth scale these are relatively shallow at 30–90 pm-km. The one notable exception is the Zero integration that shows a steady increase from $\sim L = 100$ (17 pm-km), but the magnitude of this increase is only about 10 mGal at $L = 10$, compared to hundreds of mGal under the basins (see also our discussion above). Table 1 lists the basins, their locations, Bouguer diameters, crustal thickness, age class, the degree of the transition depth, the depth of the transition (pm-km) (the depth of the primary component of the basin anomaly), the gravity signal (mGal) at the transition, and the estimated ranges by Liang et al. (2014; 10–50 km) and Zhao et al. (2019, 2021; base of the crust to 80 km). The uncertainties for the transition level were derived from the rms of the gravity about the transition level based on a low-degree polynomial fit to 20–30 degrees of *L* about the transition level.

Our transition depth is within the ranges of seven of the nine basins that are in common with the depth ranges of Zhao et al., indicating that our method, which does not depend on additional constraints, obtains results similar to an inversion analysis with a different approach. The two basins that are outside this range (shown in red) are Imbrium and Serenitatis on the nearside.

Figure 10 shows the relationship between the transition depth and the other parameters in Table 1 for all 19 basins except SPA. Figure 10(a) shows two populations selected according to their transition depth being shallower or deeper than the average transition depth of 33 km, which we note is close to the average crustal thickness. One group increases linearly with latitude with minimal scatter; the other shallower-depth basins show minimal change with latitude. Figure 10(b) shows that a cosine fit, including phase, to the combined populations appears associated with longitude, one group on the lunar nearside, the other group on the lunar farside, suggesting that the shallower transition depth is probably the result of their being in the thicker farside highlands. This could also be related to differences in thermal properties between the nearside and farside resulting in different basin sizes (Miljković et al. 2013), where the nearside larger basins end up deeper than farside basins. Figures 10(c) shows that there is a linear relationship between the transition depth and the Bouguer diameter of the anomaly with pm-km depth-to-diameter ratio of ~ 0.1. This ratio is similar to that between topographic depth and topographic diameter of craters and could be a result of the impact that formed the basin. In addition, as mentioned above, it also indicates that the transition degree is also a measure of the feature being resolved at the surface.

Figures 10(d) and (e) show that the grouping persists when plotted against crustal thickness and anomaly magnitude; Figure 10(f) shows that the magnitude of the anomaly at the transition depth is linearly related to the crustal thickness such that the larger the anomaly the shallower the crustal thickness.
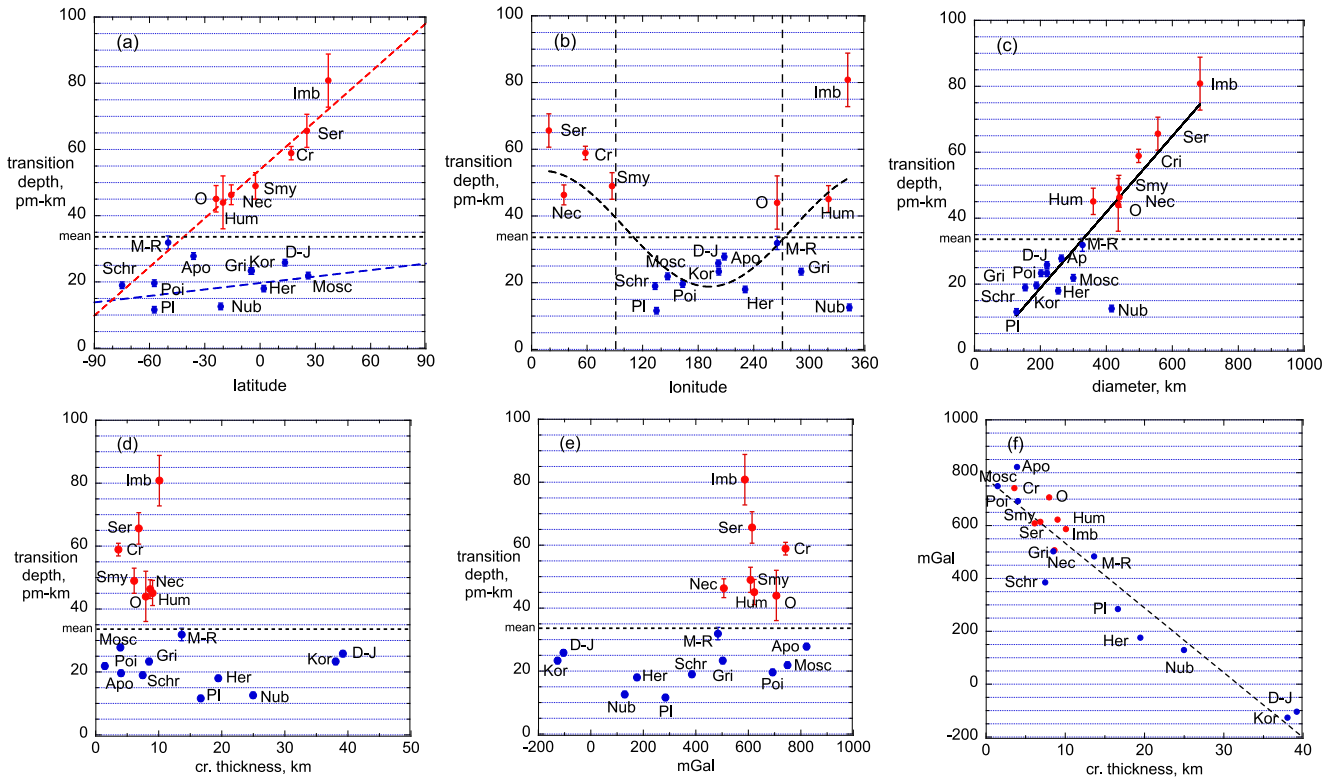
Figure 10. Relationship between transition depth and basin location, diameter, crustal thickness, and anomaly magnitude. (a) Latitude; (b) longitude; (c) diameter; (d) crustal thickness; (e) anomaly magnitude; (f) anomaly magnitude vs. crustal thickness. The lines are best fits to the uniformly weighted data, including panel (b), which has amplitude and phase estimated.

From Figure 10(d) it is clear that for most basins the transition depth is greater than the local crustal thickness, placing the representative depth of the mass anomaly in the mantle (while still noting that our derived depth can be considered a maximum depth). This is the case for 14 of the basins, including SPA. We also note that most of these basins could have excavated mantle material, based on the distribution of olivine (Miljković et al. 2015).

3.2. Horizontal Constraints: Slices

The cumulative gravity spectra provide an estimate of the depth of the primary gravity features, but not their extent laterally. We investigate the geographical extent of the gravity anomalies by studying horizontal "slices," where a "slice" is presented as a geographical map of a feature for a specific range of spherical harmonic degrees (band-filtered). Another way of looking at this is that a slice presents a collection of profiles in a geographical area, collapsed for a range of degrees. The relationship of center spectra to horizontal slices is shown in Figures 11 and 12 for Orientale, Mendel–Rydberg, Imbrium, and Serenitatis.

In both Figure 11 and 12 we see that most of the signal is contained in two low degree ranges, $L = 6$–29 (57–231 pm-km) and 30–60 (29–55 pm-km), both shown with a gravity range of -600 to 1000 mGal. The other figures, which have gravity ranges of only ± 50 and ± 20 mGal, contribute much less to the total gravity but appear to show structure of the anomaly, as in degrees 60–89 (19–28 pm-km) and 30–59 (29–55 pm-km). The explanation of the circular structures is believed to be ringing associated with the degree band: a hard cutoff of degrees can result in ringing due to the spherical harmonics, as

only certain wavelengths are included. This, of course, is the case for any slice; it appears that the range 60–89 is especially prone to this.

As mentioned earlier, from simulations of an anomaly, we believe that the patterns represent the limits of spatial resolution for specific degree bands. At the surface the spatial resolution for degree 540 is about 10 km, so any feature smaller than $\sim$10 km is not resolvable; at degree 180 the spatial resolution is about 30 km and only features larger than 30 km are resolved. For Figures 10 and 11 in the $L = 60$–89 band the resolution matches the spatial resolution, enabling us to see the effects of ringing in this degree band of 19–28 pm-km. We believe that this explains the presence of the patterns in bands that do not fully resolve the basin.

The overall conclusion from Figures 11 and 12 is that gravitational structure beneath Orientale, Mendel–Rydberg, Imbrium, and Serenitatis suggests changes with depth, and that density variations below all major impact basins exhibit broad similarities. All four anomalies show a smooth central region close to the surface, and all gravity resulting from the impact is contained within $\sim$150 pm-km ($L \sim 10$) of the surface. Figure 2 indicates that it is also likely true for most of the basins with the possible exception of SPA.

3.3. South Pole–Aitken

Figures 2 and 4 show little variation in gravity anomaly signal of SPA for degrees of $L > 10$, but Figure 4 shows that SPA has a transition depth at $L = 7$, $\sim$204 pm-km and that the pm-km depth of the transition is $\sim$0.1 of its diameter, which is approximately the value of transition depth of SPA (Figure 10, text). SPA for $L > 10$ appears to be more like the Zero
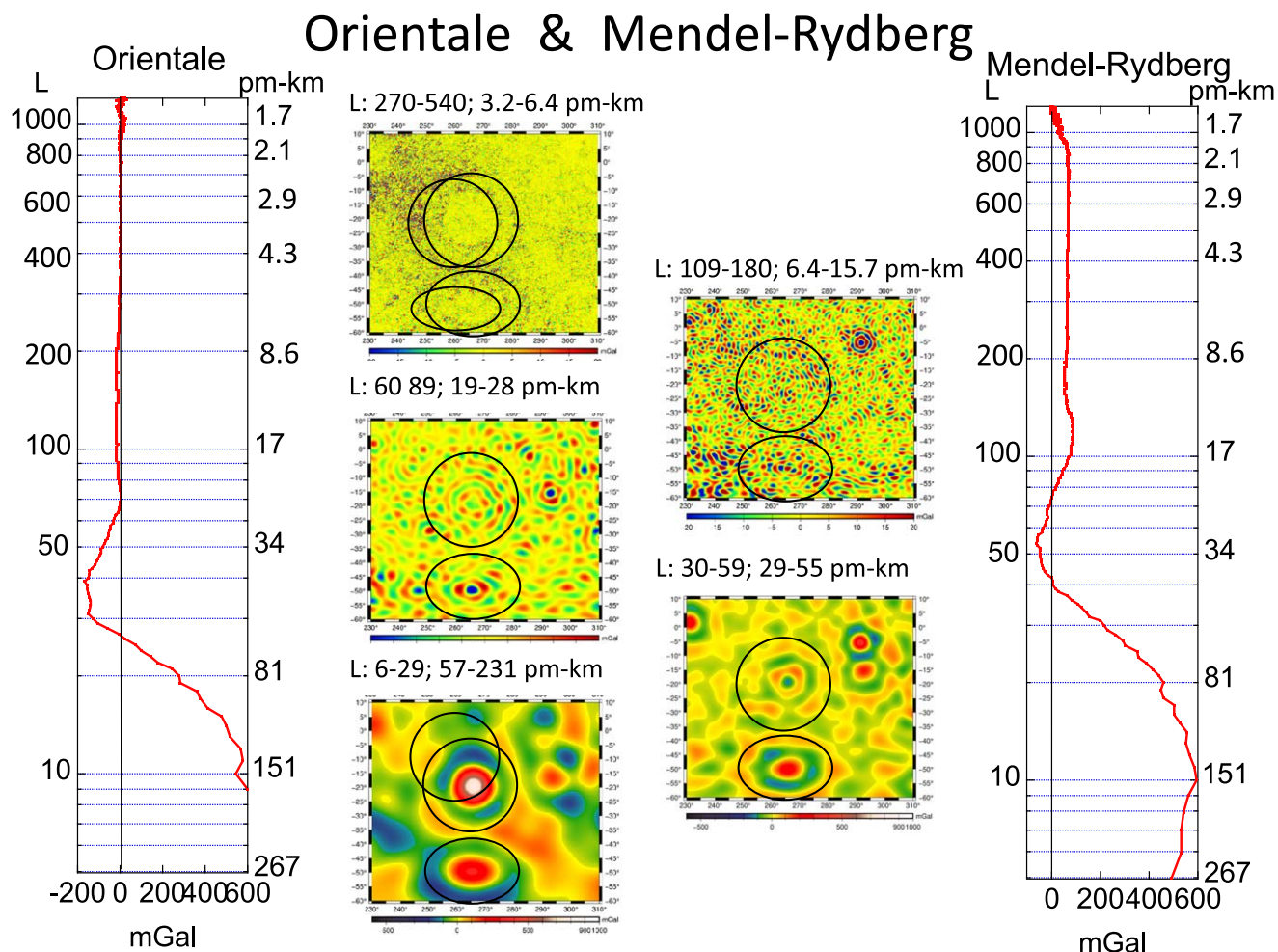
Orientale & Mendel-Rydberg

Figure 11. Example of relationship of spectra to horizontal slices for 5 degree bands 270–540, 109–180, 60–89, 30–59, and 6–29 and corresponding pm-km depth under Orientale and Mendel–Rydberg. The longitude scale is 230–310, latitude scale 60S–10N; the color scale is ±20 mGal for the top two slices, ±50 mgal for the center image, and −600 to 1000 mGal for the lower two slices. Also seen are the Grimaldi and Cruger basins in the upper right corner of the slices. Quasi-circular outlines have been inserted in the figure for ease of comparison of slices and are carried through all degree ranges. The spectra are cumulative, integrated downward from the surface ($L = 1200$).

spectrum than other basins, while recognizing that the Zero spectrum has a much smaller amplitude. This suggests that SPA is likely to be more homogeneous over depth than other basins, consistent with it being old and largely compensated (Spudis et al. 1994; Zuber 1994).

Figure 13 shows eight slices through SPA with the basin shape from Garrick-Bethell & Zuber (2009). Common through all the slices are the fewer anomalies seen in the central region of SPA, with values of zero or near-zero mGal in each slice. In the 271–540 degree band, representing the near-surface region, 3.2–6.4 pm-km, the Bouguer shows the clear boundary of gravity of the SPA depression. The topography of the central region of SPA is ∼6 km below the reference level, rising to ∼4 km below the reference level at latitude –80 and to ∼0 km on the northern edge of the elliptical center and eventually rising to ∼6 km above the reference level in the northern highlands. This difference in topography reduces the resolution of the gravity, compared to the higher elevations, and the observability of small anomalies, although it should be noted that the local resolution of the gravity field models in SPA is still at degree 540 or so (Goossens et al. 2020). However, the lack of anomalies continues to at least $L = 60$ (∼28 pm-km), with some individual anomalies appearing in the central region, where the gravity

field for these degrees is extremely well determined. This suggests that the lack of (major) anomalies is most likely the result of the region being relatively homogeneous from the surface down to 20–30 km. Mass excesses at shallower depths such as the mafic mound (Moriarty and Pieters 2015) are known to exist, and the slices in this depth range indicate clusters. Such smaller features are not included in this analysis.

The large gravity signal situated at depth under SPA at >200 km is in agreement with James et al. (2019) and Trowbridge et al. (2020). This result is also consistent with the low Bouguer gravity of SPA seen in Figure 1(b).

3.4. Hemispheric Views

Figure 14 shows projections of the northern and southern hemispheres for eight degree bands and depths. The shallowest two depths, 3–6 pm-km (top row, 1 and 3), show no major anomalies within this band except surrounding 8–10 large basins, many not discussed in this paper, but all possessing a paucity of smaller anomalies in their interior. At 10–16 km depth (top row, 2 and 4), several of the basins are no longer evident, including Orientale. At 29–55 pm-km (lower row, 1 and 3), the basins are clearly defined by their circular pattern seen previously in Figures 12–14, but with a different color

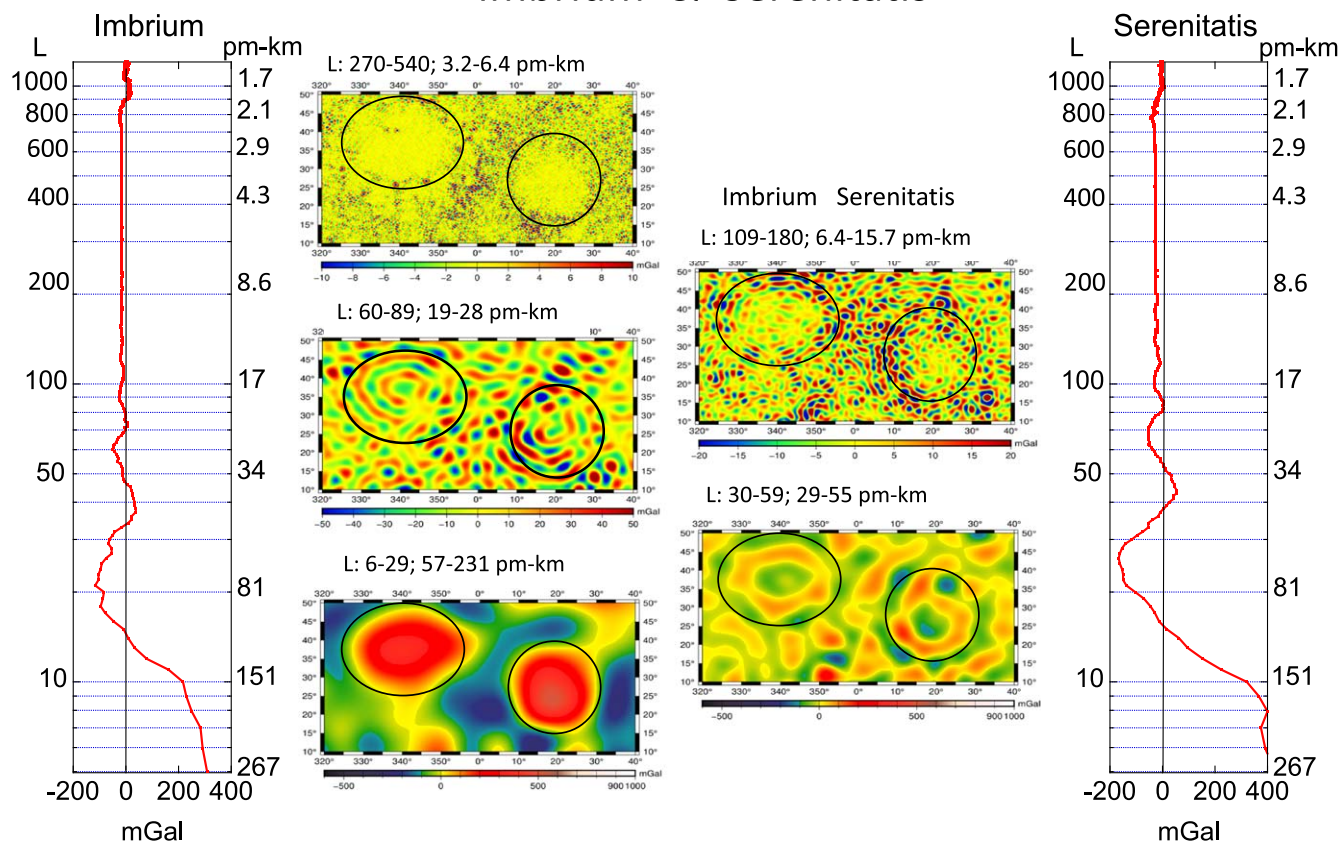THE PLANETARY SCIENCE JOURNAL, 4:204 (14pp), 2023 November

Smith et al.

Figure 12. Bouguer slices for 5 degree bands for the Imbrium and Serenitatis basins. Each slice shows how the anomaly varies in apparent structure over each depth range and contributes to the total field of the anomaly (Figure 1b). The longitude scale is 320–40, and the latitude scale is 10N-50N; the color scale is ±20 mGal for the top two slices, ±50 mgal for the center image, and −600 to 1000 mGal for lower two slices. Quasi-circular outlines have been inserted in the figure for ease of comparison of slices and are carried through all degree ranges. The spectra are cumulative, integrated downward from the surface ($L = 1200$).

palette. At depths >150 pm-km (lower row, 2 and 4), the structure of only the major basins is identifiable. In the southern hemisphere it is exclusively SPA, consistent with the transition depth at ∼200 km. The same caution and discussion with respect to ringing and to resolution are appropriate for the interpretation of Figure 14.

4. Summary of Spectral Method and Assumptions

We have analyzed the lunar gravity field (1200B; Goossens et al. 2020) by studying the variation of Bouguer gravity with spherical harmonic degree. We use the approximate relationship between spherical harmonic degree and depth (Goossens & Smith 2023) to provide the structure of the gravity signal with depth in pm-km, the depth based on a point-mass representation. The gravity is evaluated at 1738 km with a crustal density of 2500 kg m^{-3}. We analyze the gravity spectra for the degree range 2–1200, for both the individual and the cumulative spectra. We use pm-km for the depth to indicate that it is based on a model, but we believe the model to be a reasonable estimate of the maximum depth of the anomaly.

5. Summary of Observations and Conclusions

1. We define the depth of the primary contribution to the gravity field of a basin as the "transition depth" where the cumulative gravity reaches a maximum and represents the spherical harmonic degree of the positive Bouguer anomaly below the surface. We approximate its

maximum depth in km from the pm-km relationship of Equation (1).

2. The depth (transition level) of the positive mass anomaly under a basin depends on longitude; nearside basins are deeper (>35 pm-km) by a factor of ∼2 compared to the farside ones (<35 pm-km), excluding SPA.

3. The transition depth of nearside basins depends on latitude: shallower in the south, and deeper in the north.

4. The transition level is directly related to the diameter of the basin in an approximate ratio of depth (pm-km) to diameter (km) of ∼0.1 and consistent with it being an effect of basin diameter relative to the horizontal resolution of the spherical harmonics.

5. The transition level is greater than the crustal thickness for 14 basins, including SPA, placing the maximum depth of the mass anomaly in the mantle. The exceptions are Dirichlet–Jackson, Hertzsprung, Korolev, Nubium, and Planck; these are all on the lunar farside, with the exception of Nubium, and likely due to the smaller sizes of basins on the farside.

6. The spectra appear to suggest three gravitationally distinctive regions beneath a basin: (1) $800 > L > 100$ (∼3–17 pm-km) is benign, showing only very small anomalies, suggesting a possible mixing and relaxation of the near-surface melt comminuted with ejecta infall, combined with homogenization associated with post-basin formation impact bombardment; (2) a central region ($100 > L > 30$, ∼17–55 pm-km) showing quasi-periodic
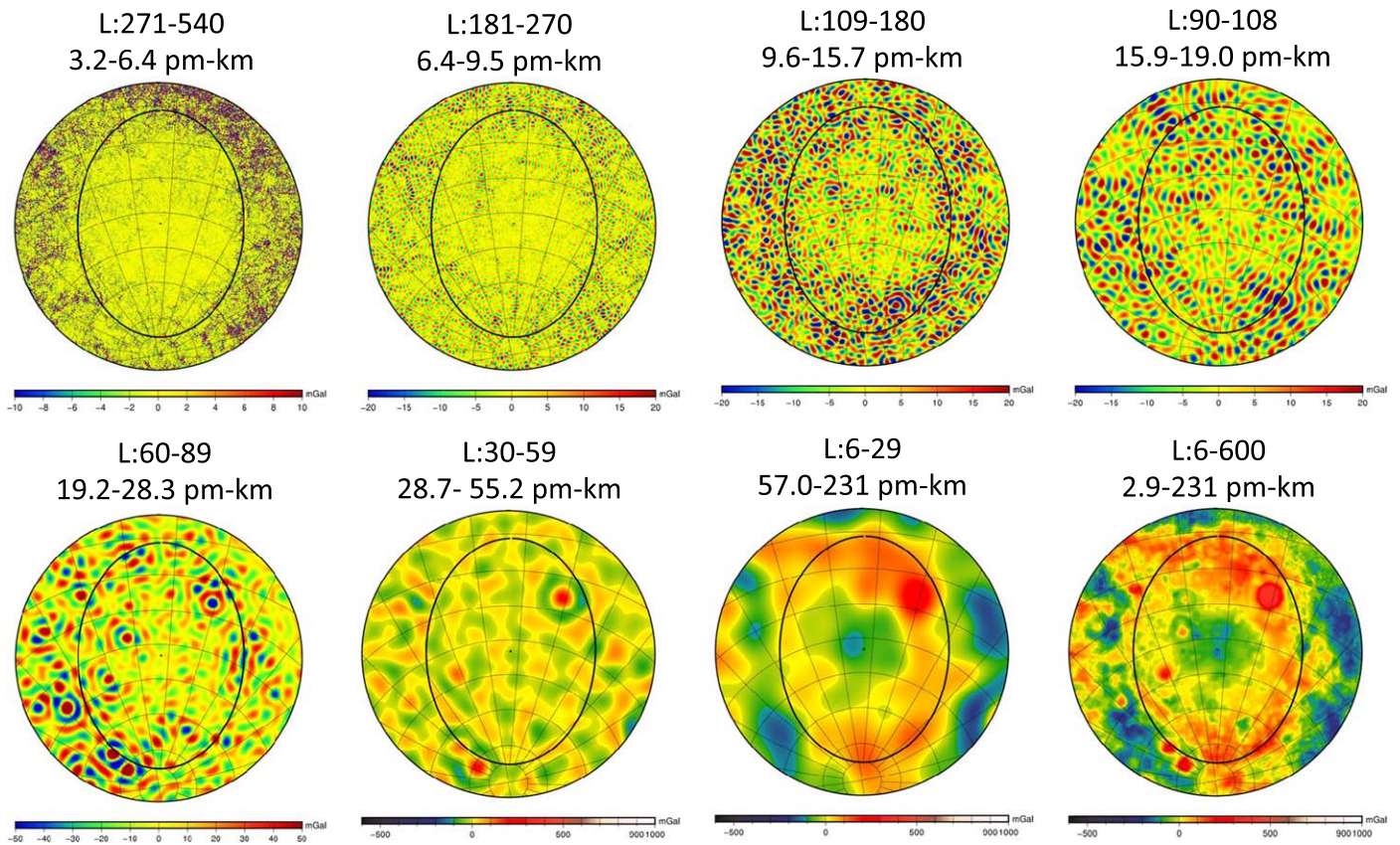
Figure 13. Planviews of SPA projected from the center of the basin showing eight slices though the basin center. In all slices the value at the center is zero or near zero, consistent with the individual spectrum in Figure 2. The maps are in stereographic projection centered on 190°E, 54°S, spanning a radius of 40°.
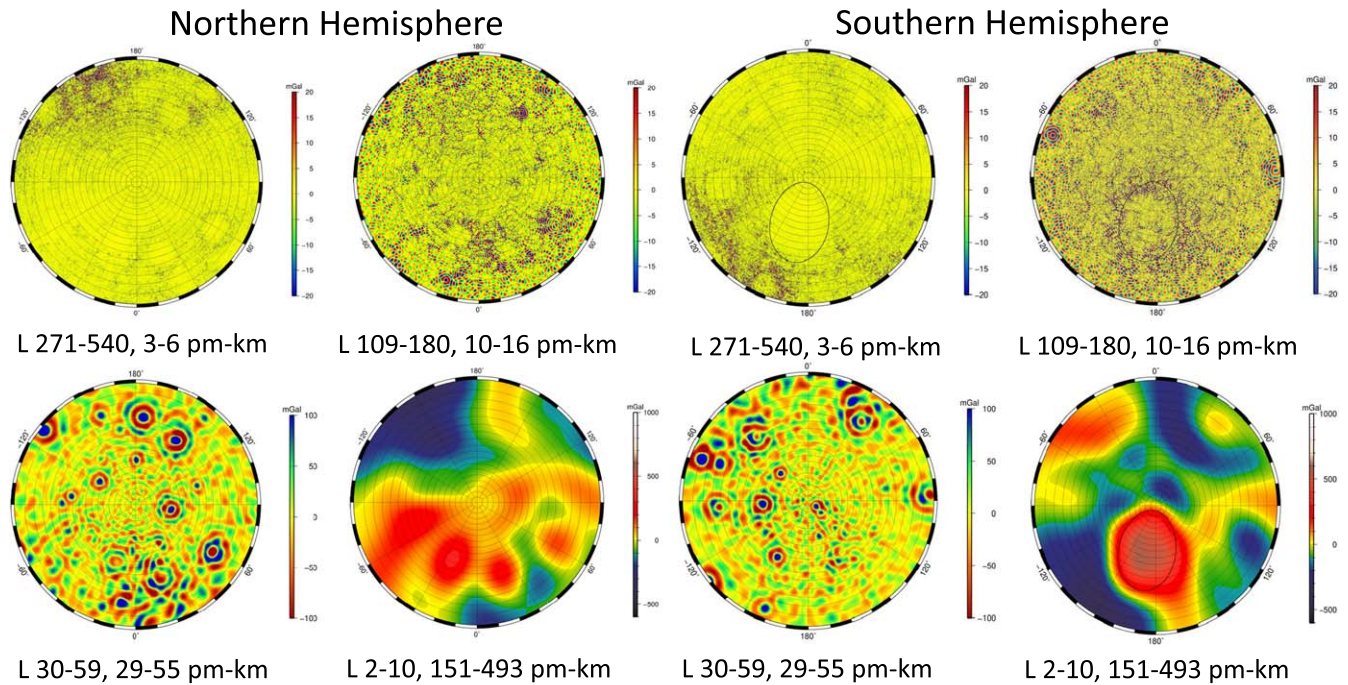

Figure 14. Hemispheric slices through the NH and SH. The figures show the gravity signal at 3–6, 10–16, 29–55, and 150–493 pm-km. The maps are stereographic projections centered on each pole and extend to the equator.

variations, which we suggest are largely due to ringing, and possible density variations that could be the result of the original impact and subsequent readjustment; and (3) a deeper region that produces the main surface gravity

signal prior to merging with the deep interior at $L \sim 10$, $\sim$250 km.

7. SPA spectra, together with band-filtered gravity, in contrast to the other basins, show the primary location

of a mass anomaly at much greater depth, $\sim$204 pm-km, $L = 7$, effectively the horizontal resolution of the basin, and in general agreement with James et al. (2019) and consistent with SPA being compensated as evidenced by negligible free-air gravity.

8. The Zero spectrum, the mean spectrum of over 15,000 locations where the Bouguer gravity is zero ± 1 mGal, shows no anomalies and no transition level. We interpret this as the "normal" Moon in the absence of major impacts and it is the spectrum of a body that has a largely spherical deep interior (below 250 pm-km, $L < 5$).

9. In a comparison with Zhao et al. (2021), we find that our transition level falls within the depth range of their increased density contrasts for seven out of nine basins in common, the exceptions being the nearside basins, Imbrium and Serenitatis, where we find the greatest anomaly depths.

10. The maximum anomaly depths of 18 basins lie within the top 80 pm-km of the surface, and all 18 gravity spectra merge with the deep interior at $L \sim 10$, $\sim$150 pm-km. SPA is the exception. These observations indicate the probable depth penetration of disruption of the density structure of the lunar interior associated with impact bombardment.

Acknowledgments

ORCID iDs

David E Smith ● https://orcid.org/0000-0003-3104-2169
Sander Goossens ● https://orcid.org/0000-0002-7707-1128
Gregory A Neumann ● https://orcid.org/0000-0003-0644-9944
Maria T Zuber ● https://orcid.org/0000-0003-2652-8017

References

Andrews-Hanna, J. C., Asmar, S., Head, J. W., III, et al. 2013, Sci, 339, 675
Andrews-Hanna, J. C., Besserer, J., Head, J. W., III, et al. 2014, Natur, 514, 68
Andrews-Hanna, J. C., Head, J. W., Johnson, B. C., et al. 2018, Icar, 310, 1
Besserer, J., Nimmo, F., Wieczorek, M. A., et al. 2014, GeoRL, 41, 5771
Bowin, C. 1983, MarGe, 7, 61
Bowin, C. 1986, Geop, 51, 123
Dehlinger, P. 1978, Marine Gravity, Vol. 22 (Amsterdam: Elsevier)
Evans, A. J., Soderblom, J. M., Andrews-Hanna, J. C., Solomon, S. C., & Zuber, M. T. 2016, GeoRL, 43, 2445
Garrick-Bethell, I., & Zuber, M. T. 2009, Icar, 204, 399
Gong, S., Wieczorek, M. A., Nimmo, F., et al. 2016, JGRE, 121, 854
Goossens, S., Sabaka, T. J., Wieczorek, M. A., et al. 2020, JGRE, 125, e2019JE006086
Goossens, S., & Smith, D. E. 2023, GeoJI, 233, 1878
Han, S.-C., Schmerr, N., Neumann, G. A., & Holmes, S. 2014, GeoRL, 41, 1882
Heiskanen, W. A., & Moritz, H. 1967, Physical Geodesy (San Francisco, CA: W.H. Freeman and Company)
James, P. B., Smith, D. E., Byrne, P. K., et al. 2019, GeoRL, 46, 5100
Jansen, J. C., Andrews-Hanna, J. C., & Li, Y. 2017, Icar, 291, 107
Li, Y., & Oldenburg, D. W. 1998, Geop, 63, 109
Liang, Q., Chen, C., & Li, Y. 2014, JGRE, 119, 1359
Kaula, W. 1966, Theory of Satellite Geodesy. Applications of Satellites to Geodesy (Waltham, MA: Blaisdell)
Losiak, A., Wilhelms, D., Byrne, C., et al. 2009, LPSC, 40, 1532
Melosh, H. J., Freed, A. M., Johnson, B. C., et al. 2013, Sci, 340, 1552
Milbury, C., Johnson, B. C., Melosh, H. J., et al. 2015, GeoRL, 42, 9711
Miljković, K., Wieczorek, M. A., Collins, G. S., et al. 2013, Sci, 342, 724
Miljković, K., Wieczorek, M. A., Collins, G. S., et al. 2015, E&PSL, 409, 243
Moriarty, D. P., III, & Pieters, C. M. 2015, GeoRL, 42, 7907
Muller, P. M., & Sjogren, W. L. 1968, Sci, 161, 680
Neumann, G. A., Zuber, M. T., Wieczorek, M. A., et al. 2015, SciA, 1, e1500852
Pollack, H. N. 1973, JGR, 78, 1760
Smith, D. E., Zuber, M. T., Neumann, G. A., et al. 2016, Icar, 283, 70
Soderblom, J. M., Evans, A. J., Johnson, B. C., et al. 2015, GeoRL, 42, 6939
Sori, M. M., Zuber, M. T., Head, J. W., & Kiefer, W. S. 2016, Icar, 273, 284
Šprlák, M., & Han, S.-C. 2021, ESRv, 222, 103739
Spudis, P., Gillis, J. J., & Reisse, R. A. 1994, Sci, 266, 1848
Sutton, S. T., Pollack, H. N., & Jackson, M. J. 1991, GeoJI, 107, 77
Trowbridge, A. J., Johnson, B. C., Freed, A. M., & Melosh, H. J. 2020, Icar, 352, 113590
Wieczorek, M. A. 2015, in Treatise on Geophysics, Second Edition, ed. G. Schubert (2nd ed.; Amsterdam: Elsevier)
Wieczorek, M. A., Neumann, G. A., Nimmo, et al. 2013, Sci, 339, 671
Wieczorek, M. A., & Phillips, R. J. 1998, JGR, 103, 1715
Zhao, G., Chen, B., Uieda, L., et al. 2019, JGRB, 124, 4157
Zhao, G., Liu, J., Chen, B., Kaban, M. K., & Du, J. 2021, JGRE, 126, e2021JE006841
Zuber, M. T., Smith, D. E., Lemoine, F. G., & Neumann, G. A. 1994, Sci, 266, 1839
Zuber, M. T., Smith, D. E., Lehman, D. H., et al. 2012, SSRv, 178, 3
Zuber, M. T., Smith, D. E., Watkins, M. M., et al. 2013, Sci, 339, 668
Zuber, M. T., Smith, D. E., Neumann, G. A., et al. 2016, Sci, 354, 438